How faceted liquid droplets grow tails

Supplementary Material

Shani Guttman [*], **Zvi Sapir** [*] [†], **Moty Schultz** [*], **Alexander V. Butenko** [*], **Benjamin M. Ocko** [‡], **Moshe Deutsch** [*] **and Eli Sloutskin** [*]

[*]Physics Department & Institute of Nanotechnology and Advanced Materials, Bar-Ilan University, Ramat-Gan 5290002, Israel,[†]Current address: Intel (Israel) Ltd., Kiryat Gat, Israel, and [‡]Condensed Matter Physics & Materials Sciences, Brookhaven National Laboratory, Upton, NY 11973, USA

Submitted to Proceedings of the National Academy of Sciences of the United States of America

Supplementary Materials and Methods

Chemicals. C_{18}TAB (Aldrich, $\geq$ 99 % and $\geq$ 98 % pure) was recrystallized 1-3 times from a methanol - acetone solution. C_{16} alkane, hexadecane, (Aldrich, 99 % pure) was percolated 2-3 times through fresh activated basic alumina columns to remove polar components. Millipore Ultrapure 18.2 MΩ-cm water was used throughout.

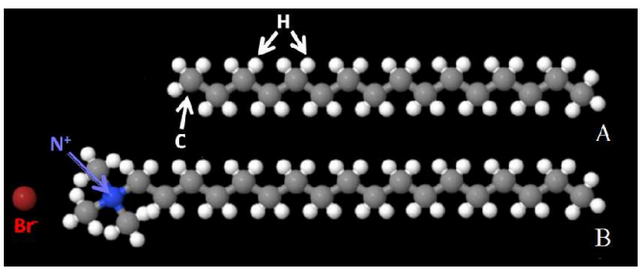

Fig. S1. Molecular structure. (A) Hexadecane (C_{16}) normal-alkane, $CH_3(CH_2)_{14}CH_3$. (B), Trimethyloctadecylammonium bromide (C_{18}TAB or STAB) surfactant, CH_3-$(CH_2)_{17}N(CH_3)_3Br$. All chemical bonds are covalent except for the bromine, which has an ionic bond with the nitrogen. Color code: carbon - grey, hydrogen - white, nitrogen - blue, bromine - brown.

In planar interfaces measurements, as also in some of the emulsion measurements, all parts of the equipment coming in contact with the sample have been soaked in hot Piranha solution, a widely-used method for removing organic impurities. However, the large interfacial area of the emulsions significantly reduces the sensitivity of the measurements to impurities. Moreover, the ultralow γ in these emulsions renders interfacial adsorption of impurities energetically unfavorable. Therefore, cleaning the equipment with common organic solvents was found to yield identical results to Piranha cleaning.

Emulsions are prepared by mixing 0.05% of C_{16} in 0.3 mM to 1 mM water solution of C_{18}TAB, and stirring at 50°C for ∼5 minutes for $\sim$ 100 μm droplets and for $\sim$ 12 hours for $\sim$ 10 μm droplets, employing a hotplate/magnetic stirrer. The interface/bulk mass ratio in these emulsions is high; therefore, the concentration of C_{18}TAB in the bulk aqueous phase drops during stirring as the C_{16} droplets get smaller and the total oil-water interfacial area grows. Thus, we disperse a small amount of the prepared emulsion in a large volume of a C_{18}TAB aqueous solution, where the concentration was 0.6, 0.7, or 0.8 mM; all results stay unchanged in this concentration range. This re-dispersion procedure, significantly reduces the sensitivity of the shape transition temperatures to the details of the emulsion preparation process. No crystallization of the surfactant is observed in the relevant temperature range.

Optical microscopy. The emulsions are loaded by capillary forces into Vitrocom® $0.1 \times 2 \times 50$ mm rectangular glass capillaries and sealed by an instant Epoxy glue. $0.6 \times 0.6 \times 50$ mm capillaries were used for the largest droplets. Unsealed samples, contained between two glass slides, yield similar results except for having a much-reduced stability and not allowing measurements of large droplets. The capillary is glued with its wide face down onto an aluminum slide, having a narrow machined opening for optical observations. The slide is inserted horizontally into a home made temperature-controlled cell, mounted on the translation stage of an inverted microscope. The sample cell employed a pair of Peltier elements for baseplate cooling, and a Lakeshore model 330 for PID temperature control via thin-film resistive heaters. Where oil-immersed objectives were used for imaging, their temperature was controlled by the Okolab® temperature control system, based on a water circulator. Our setup allows the temperature of the sample to be regulated to 0.01 °C, in the range from 10 to 50 °C. At low temperatures, where water condensation from air interfered with the imaging, the experimental setup was covered by a plastic bag, inside which a dry nitrogen atmosphere was maintained.

Bright-field microscopy was carried out employing an inverted Nikon Ti-E microscope, with a Nikon DS-Fi1 CCD installed for video acquisition. The microscope is part of a Nikon A1R scanning confocal setup, allowing either bright-field, phase contrast, DIC, or confocal measurements to be carried out. Most measurements have been carried out in the bright-field mode. For confocal images, the oil was fluorescently labeled with the Bodipy 505/515 hydrophobic dye, which was then excited by the 488nm line of the Ar laser. The droplets float up in water by buoyancy, so that an upright or horizontal optical axis microscopy proved optimal in some cases. In these cases, we rotated the optical axis employing an InverterScope® objective inverter. The images were taken by Plan Apo 100x (NA=1.4), Plan Apo λ 100x (NA=1.45), and 60x (NA=1.4) oil-immersed objectives. Where more careful temperature determination was needed, we employed a dry Plan Fluor 100x (NA=0.9) objective, which does not touch the sample capillary.

Three-dimensional confocal imaging was carried out in a resonant scanning mode, with the 512×512 pixel frames collected

Reserved for Publication Footnotes

at ∼7 fps. A piezo device was employed for rapid scanning of the sample along the optical axis. The voxel size in confocal measurements was typically chosen as $0.06 \times 0.06 \times 0.4$ μm^3, slightly oversampling the optical resolution with the confocal pinhole size set to $0.8 - 1$ AU. In general, interfacial phenomena are highly sensitive to contaminations, such that the fluorescent staining for confocal microscopy may significantly disturb the behavior of the system[1]. The non-polar Bodipy-505/515 dye, used in these studies, is among the very few fluorescent dyes which are strongly hydrophobic and do not adsorb to charged oil-water interfaces. However, even with this dye, strong irradiation by the laser source results in its photoinduced ionization, after which the dye adsorbs to the interface, enhancing the spontaneous emulsification phenomena. To avoid these artifacts as much as possible, all but a few of the results in this work are based on the bright field microscopy, where fluorescent dye was not used.

For the preparation of the current manuscript, we measured many hundreds of droplet shapes. Still, within the available statistics, we could not see any significant variation of shapes across the statistical ensemble. Thus, the free energy minima of the system must be narrow and much deeper than 1 k_BT. Importantly, the buckling temperature T_d depends on the size of the droplets, as demonstrated in Fig. S2. This dependence was used to obtain the data in Fig. S4, as described below.

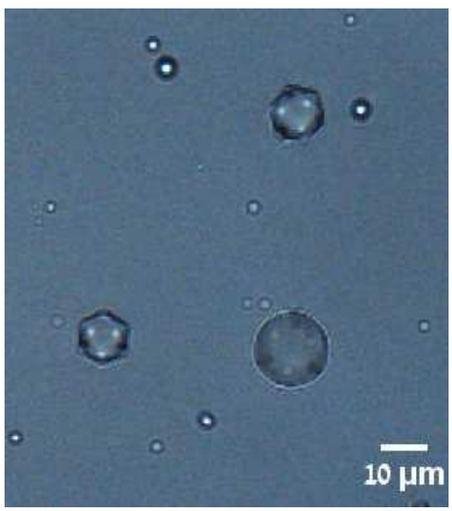

Fig. S2. A typical bright field image of an emulsion demonstrates the dependence of the buckling transition temperature T_d on droplet radii. The temperature of this image was set such that the largest droplet is on the verge of converting into an icosahedron, while the smaller droplets already have well-developed icosahedral shapes. The smallest droplets in this image are below optical resolution, so that their shapes cannot be resolved.

Macroscopic γ measurements. The Wilhelmy plate method, well documented in the literature[2, 3, 4, 5], was used to measure the interfacial tension of the planar buried oil-water interfaces, employing a glass plate of 41-mm circumference. The pendant drop tensiometry employed a home-built temperature-regulated cell, electronically controlled to 0.01 °C, mounted on a commercial Dataphysics® OCA20 optical shape-measuring system operated in the pendant-drop mode. We re-scaled the drop tensiometry data slightly to make the slope of $\gamma(T)$ at $T > T_s$ match the Wilhelmy plate result; this accounts for the slow rate of C_{18}TAB adsorption onto the interface of a newly-created drop.

Microscopic γ measurements. For optical microscopy, the emulsion is loaded into a glass capillary (see Optical Microscopy section, above). The liquid C_{16} droplets float to the capillary's top wall, under the joint action of buoyancy and gravity. At $T > T_s$, where $\gamma \approx 5 \times 10^{-3}$ J/m^2, the droplet's distortion from a sphere is negligible, as demonstrated by three-dimensional (3D) confocal microscopy (Fig. S3A). Upon cooling, however, a flat circular region of a progressively larger radius r_c appears at the droplet's top (Fig. S2B), indicating squashing against the capillary wall, and thus - ultralow γ values. Gravity and buoyancy are bulk forces scaling with droplet radius R_0 as R_0^3; the Laplace pressure due to γ scales as R_0^{-1}. Thus, $r_c \propto R_0^2$ is expected and, indeed, measured (Fig. S3C), indicating that the flattening is fully described by an interplay between gravity, buoyancy, and γ. Most importantly, the observed r_c allows the temperature dependent ultralow γ of these microscopic droplets to be measured *in situ*, which is highly challenging otherwise. Specifically, for small droplet distortions[6] $\gamma = (2/3)R_0^4 \Delta\rho g r_c^{-2}$, where $\Delta\rho = 0.23$ g/cm^3 is the density mismatch between alkane and water, and $g = 9.8$ m/s^2. We plot the $\gamma(T)$ values, thus obtained, in Fig. 2 of the main text (green symbols); note the positive slope $d\gamma/dT > 0$, indicative of an interfacial freezing. Also, we obtain the γ values at the buckling transition for a range of (relatively large) droplet radii. These values match nicely the trend observed for smaller R_0, based on $T_d(R_0)$ measurements (see Fig. S4).

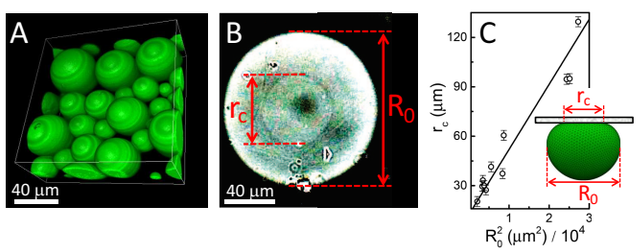

Fig. S3. Microdroplet shape analysis. Shapes of capillary-contained oil-in-water emulsion droplets are determined by the balance between gravity, buoyancy and interfacial tension γ , allowing ultralow γ values to be measured in situ. (A), At high γ, all droplets are spherical (confocal microscopy reconstruction). (B), At low γ, the topmost part of the droplets flattens as the droplet is squashed against the top wall of the capillary (see cartoon in (C)). (C), The measured contact area radii r_c of droplets of radii R_0 (symbols) follow the theoretical scaling $r_c \propto R_2^0$ (solid line). The interfacial tension γ, plotted in Fig. 2 (green symbols) of the main text, is extracted from the prefactor of this relation (see Supplementary Materials and Methods).

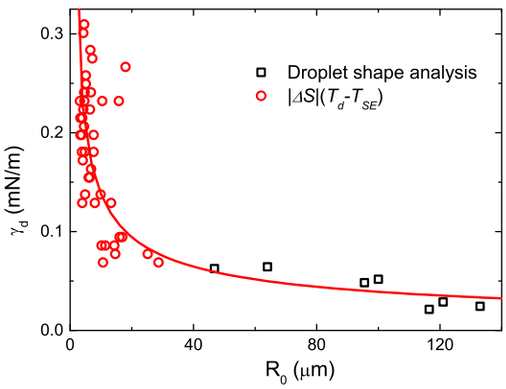

Fig. S4. The surface tension γ_d at the buckling transition temperature T_d decreases with increasing droplet radius R_0. For the largest droplets ($R_0 > 40\mu$m), the γ_d values (black squares) were obtained by optical microdroplet shape analysis (see Supplementary Materials and Methods). For the small droplets, where the buoyancy-induced distortions are too small to be reliably measured by optical microscopy, γ_d (red circles) were estimated from the buckling temperature T_d of each droplet as $T_d = |\Delta S|(T_d - T_{SE})$. T_{SE} is the temperature of spontaneous emulsification, where $\gamma(T_{SE}) = 0$. $|\Delta S|$ is the entropy loss on freezing of a C_{16} monolayer[2, 5]. Note the smooth joining of the two sets of data, strongly supporting our results. The fitted exponentially decreasing line is only a guide to the eye.

Optical tweezers. Home-built optical tweezing setup, based on a diode-pumped Nd:YAG laser (at 1064nm), was employed to test the mechanical properties of the droplets. To roughly calibrate the force F applied on the emulsion droplet by the tweezing laser, we move the sample at different velocities, and find the minimal velocity that drags the droplet out of the optical trap. The force due to the viscous Stokes drag at velocity v on a sphere of radius R_0, in a medium with a viscosity η is: $F_v = 6\pi\eta R_0 v$; this estimate yields $F_{max} \approx 4$ pN for the maximal trapping force which we can apply on a droplet of $R_0 \approx 8$ μm under typical experimental conditions. As an additional test for our tweezing setup, we prepared an heptane-in-water emulsion where the interfacial tension is ultralow. This emulsion, stabilized by 1.14mM AOT (dioctyl sodium sulfosuccinate) in presence of salt (0.05M NaCl), was studied by Ward *et al.*[7]. No interfacial freezing phenomena occur in this emulsion, so that the droplets are readily deformed at low γ. Pulling an emulsion droplet at a velocity of 25 ± 1 μm/s, stretches the droplet, so that the aspect ratio of a droplet of $R_0 \approx 8$ μm reaches ~ 1.2 under steady state conditions. Balancing the Laplace pressure by the Stokes drag[7]: $\gamma = F_v bR_0/[\pi a(2ab - bR_0 - aR_0)]$, where a and b are the semi-axes of the stretched droplet, we obtain an ultralow value for the interfacial tension of the droplet $\gamma \approx 8 \times 10^{-6} N/m$, of the same order of magnitude as Ward *et al.*[7], confirming the validity of our analysis.

Computer simulations. Computer simulations have been carried out using the Surface Evolver software[8]. The droplet interface was described by a set of triangulation vertices. An icosadeltahedral triangulation lattice was used, including 12 frozen 5-fold defects[9, 10] located at the icosahedral positions. The edges are Hookean springs, with the stretching energy given by[11] $E_s = (\varepsilon/2)\sum_{\langle ij \rangle}(|\mathbf{r}_i - \mathbf{r}_j| - \tilde{a})^2$, where $\varepsilon = \sqrt{3}Y/2$, $\tilde{a}$ is the length of an unstrained edge, and the summation is carried out over all nearest-neighbor vertices. $\tilde{a}$ sets the length unit in our simulation. The bending energy is[11] $E_d = (\widetilde{\kappa}/2)\sum_{\langle IJ \rangle}(\widehat{\mathbf{n}}_I - \widehat{\mathbf{n}}_J)^2$, where $\widetilde{\kappa} = 2\kappa/\sqrt{3}$, and the summation is over all nearest-neighbor plaquettes of the triangulated surface, with unit normals $\widehat{\mathbf{n}}_I$. As in the experiment, the bulk volume of the droplets was kept constant in the simulations; importantly, bulk volume was not conserved in other theoretical studies[10] which model lipid vesicles[12, 13, 14, 15] and viruses[11] . A more complex model, where the number of defects is variable[9, 12, 16] and defects can move, is currently under construction.

Supplementary Discussion

Bright-field microscopy video of shape transitions. A typical video of a temperature scan, demonstrating the shape transitions discussed in the main text, appears in Video4.mov. The video starts with a cooling scan (00:00-00:24s), carried out at a rate of 2mK/s. Initially the central droplet is spherical. While the ~ 2 nm-thick interfacial monolayer is below the optical resolution, so that no visible changes occur at $T = T_s$, this monolayer drives the buckling at $T < T_d$ (00:15s), with the droplet adopting an icosahedral shape. On further cooling, γ switches sign from positive to (transiently) negative for $T < T_{SE}$ (00:20s), causing the onset of spontaneous emulsification (SE). Note the sharp edges of the droplets (00:20-01:14s), which contrast conventional SE, where all interfaces are diffuse and disordered. Note the tails emanating from the largest droplet, which become thinner as they grow, forming nano-coils. Significant active (non-Brownian) motion occurs in the SE regime, driven by the (transiently) negative γ. The dramatic increase in the interfacial area of the emulsion at $T < T_{SE}$ leads to surfactant depletion, so that the largest droplet becomes rounded (00:37s - 01:14s). Upon reheating to $T > T_d$, the droplets turn spherical. The heating scan, carried out at a rate of 15 mK/s, starts at 01:12s. Note that the sizes of reheated droplets are smaller than at 00:00s, as the reheating process breaks up the nano-coils, forming new droplets.

In the SE regime, where $\gamma < 0$, droplet splitting events are occasionally observed, since an increase in the total oil-water interfacial area is now thermodynamically favored. One such event is shown in Video3.mov, where a large triangular droplet splits, forming three smaller droplets.

Confirming the liquid nature of the droplets' bulk phase. Optical microscopy and optical tweezing measurements have been carried out to rule out the possibility that the shape changes observed are due to crystallization of the droplet's bulk. For comparison, fully-frozen droplets of alkane in water have been prepared, employing C_{22} (docosane) as an oil and C_{16}TAB (cetyltrimethylammonium bromide) as a surfactant. The emulsion was prepared at an elevated temperature ($T = 50$ °C); on cooling to room temperature, C_{22} droplets fully solidified. The bulk of these droplets looks inhomogeneous under either bright-field (panel **b** in Video1.mov) or polarized microscopy, and can be readily distinguished from our interfacially-frozen droplets, the liquid bulk of which appears uniform. Nematic or smectic phases of alkanes are birefringent and would have been readily detected by polarized light microscopy; no optical activity could be detected for our interfacially-frozen emulsion droplets, indicating, again, that they are simple liquids.

We also compared the response to trapping forces of a fully frozen droplet of C_{22} ($R_0 \approx 5$ μm) to the response of a faceted liquid droplet of C_{16}. In both cases, we fix the trap position (denoted by an $\times$ symbol in the movie clips) and move the sample stage. As we demonstrate in Video1.mov (panel **b**), when the solid droplet is displaced from the center of the trap

by a hydrodynamic drag, an optical restoring force immediately emerges, opposing this displacement; a balance between these two forces is achieved shortly after. Similarly, when the stage motion stops, the optical force makes the droplet return to the center of the trap. By contrast, displacing the liquid droplet from the center of the optical trap (panel **a**) does not give rise to a restoring optical force. The force emerges only when the trap is right at the boundary of the droplet, as expected from a liquid having a zero shear modulus. In conclusion, our experiments unequivocally show the bulk of the faceted C_{16} droplets to be liquid over the full temperature range employed in the present study.

Excluding wetting effects at the capillary walls. The balance of buoyancy and gravity forces on oil droplets in water pushes them up, so that the phenomena discussed in this work typically occur next to the top wall of the borosilicate Vitrocom® capillary. To confirm that the borosilicate interface does not play any significant role in the observed effects, we employed an optical trap to move the droplets away from the glass wall. These optically-trapped droplets were demonstrated to follow the same behavior as the ones sitting next to the glass wall. In particular, the droplet in Video5.mov splits at $T < T_{SE}$, forming a daughter droplet (t=50s, see the experiment time label, in the left bottom corner of the frame). The optically-trapped mother droplet, located far from the capillary walls, grows tails much like the untrapped droplets, indicating that wall interactions play no significant role in the observed phenomena. Interestingly, with $d\gamma/dT$ being positive for the interfacially-frozen emulsions (see main text), the droplets gain energy by moving away from the vicinity of the optical trap, where the temperature is slightly higher, and thus γ is higher. This "Inognaram" (inverse Marangoni) effect[17] makes the daughter droplet suck the liquid from, and thus grow at the expense of, the mother droplet ($66 < t < 76$s). Such behavior provides an additional confirmation that interfacial freezing indeed takes place in our emulsions. Finally, as the mother droplet converts into a nano-coil, the trapping force decreases, so that the nano-coil eventually leaves the trap (t = 245s).

Bending modulus: a low limit estimate based on the optical tweezing. By optically trapping a droplet while moving the sample stage at a constant velocity, the droplet is subjected to a significant hydrodynamic drag force F_v. For the droplet shown in Video2.mov, no elastic distortion is detectable by microcopy indicating that the distortion is below optical resolution. Since its past history (see Video captions) ensures that $\gamma = 0$ N/m, the droplet shape is now elasticity-dominated and any distortion observed while dragging should provide an estimate for the now-dominant bending modulus κ.

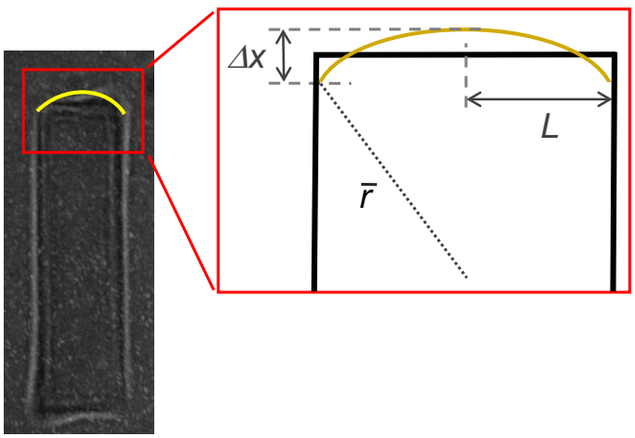

Fig. S5. Distortion of an optically-trapped droplet by hydrodynamic drag. A schematic representation of bending of the top flat facet of a droplet with a rectangular cross-section. L and Δx are defined in the magnified scheme on the right. $\bar{r}$ is the radius of curvature of the bent facet, if bending occurs.

With the viscosity of water, $\eta \approx 10^{-3}$ Pa s, and the linear dimension of a droplet, $2L \approx 8$ μm (see Fig. S5), we estimate the Stokes drag force as $F_v \approx 1$ pN, slightly lower than the maximal trapping force F_{max}, calculated above; pN forces are typical in optical tweezing experiments. To estimate the low limit on the bending rigidity κ of the frozen monolayer, we approximate the bending work done by a force F on an initially-flat surface as $F\Delta x$, where Δx is defined in Fig. S5. When $\gamma = 0$ N/m, the elastic energy cost of bending the droplet's flat facet is[18]: $E_d = 0.5\kappa\bar{r}^{-2}A_F$, where $\bar{r}$ is the curvature radius in the distorted state and $A_F \approx (2L)^2$ is the facet area. For simplicity, the distortion is assumed to be in one dimension only, as shown in Fig. S5. Relating the radius of curvature $\bar{r}$ to the distortion amplitude Δx, $(\bar{r} + \Delta x)^2 \approx \bar{r}^2 + L^2$, we obtain: $\bar{r} \approx (L^2 - \Delta x^2)/2\Delta x$. Substituting this into $E_d = F\Delta x$, yields: $\kappa \approx F(L^2 - \Delta x^2)^2/(8L^2\Delta x)$, so that κ has to be of the order of 1000 k_BT for the facet distortion to be resolvable by microscopy. A more accurate estimate has to account for the buoyant squashing of the droplets at $T < T_{SE}$; this correction would increase the estimated κ. Our calculation neglects the elastic contribution of other facets, adjacent to the one which is being bent; this contribution should decrease the estimated κ. Assuming that all these smaller corrections cancel out, κ should be larger than 1000 k_BT.

Estimation of the elastic constants. To obtain the estimates for the elastic constants in the main text, we express the elastic energy of an unbuckled monolayer with 12 five-fold defects as[11] $E_s = D + 6B\kappa\Gamma^{vK}/\Gamma_b^{vK}$, where D is a constant contribution and $B \approx 1.3$. In our case, R_0 is much larger than the lattice constant, ~ 0.5 nm, of the interfacially-frozen monolayer[3] , so that pairs of seven-fold and five-fold defects may potentially form, organized into chains[16] , or 'grain boundary scars'. Taking the scars, coupled in our case to the interfacial topology, explicitly into account is highly challenging[9, 12] . However, for a spherical surface, both the number of defect pairs and the energy of an individual pair are proportional[16] to R_0, so that the total energy scales as R_0^2.

Therefore, this contribution does not change the functional dependence of E_s on R_0.

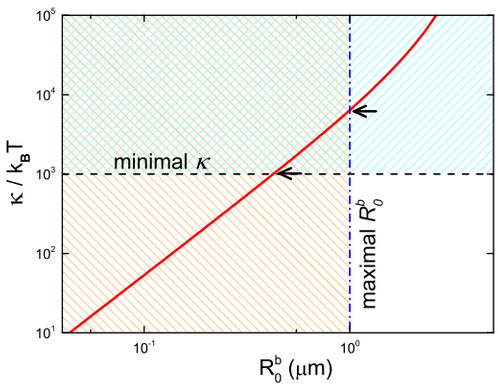

Fig. S6. Limits on γ_d, as obtained from the theory of elasticity and optical tweezing. The theoretical estimate (Eq. (1) in this document) for the bending modulus κ is plotted (red curve) as a function of R_0^b, the smallest droplet radius where buckling occurs. The curve corresponds to $R_0 = 5\mu$m, where $\gamma_b = 2.1 \times 10^{-4}$ J/m^2 (see Fig. S4). Droplets of $R_0 > 1\mu$m, sufficiently large for optical microscopy, are observed to buckle, setting the upper limit (blue dash-dotted line) on $\kappa(R_0^b)$. Thus, the physically-relevant values of $\kappa(R_0^b)$ reside in the orange-lined region. Optical tweezing experiments indicate that $\kappa > 1000\ k_BT$, limiting $\kappa(R_0^b)$ values to the orange-turquoise shaded region. The intersection of the red curve with the borders of this region yields an estimate for κ as $10^3 < \kappa < 10^4\ k_BT$. Similar plots for other R_0, within the experimental range, yield the same order of magnitude for κ .

The elastic energy in the buckled state is[11] : $E_{ico} = D + 6B\kappa[1 + \ln(\Gamma^{vK}/\Gamma_b^{vK})]$. The Gaussian rigidity is dropped in both E_s and E_{ico}, since by the Gauss-Bonnet theorem, the Gaussian curvature does not change on buckling[11] . When the interfacial elasticity is negligible, the interfacial energy difference between a sphere and an icosahedron of the same volume is $\Delta E_{int}(\gamma) = \gamma(5\sqrt{3}a^2 - 4\pi R_0^2)$, where $a = R_0\left[16\pi/(15+5\sqrt{5})\right]^{1/3}$ is the icosahedron's edge length, so that $\Delta E_{int}(\gamma) \approx 0.8\gamma R_0^2$. Denoting the interfacial tension at the onset of the buckling by $\gamma_d \equiv \gamma(T_d)$, the balance between the elastic energy and the interfacial tension is given by: $E_s = E_{ico} + \Delta E_{int}(\gamma_d)$. Substituting E_{ico} and ΔE_{int} above yields:

$$\kappa = 0.8\gamma_d R_0^2/6B[(R_0/R_0^b)^2 - 2\ln(R_0/R_0^b) - 1], \qquad [1]$$

Since $d\gamma/dT = -\Delta S$ and, by the definition of T_{SE}, $\gamma(T_{SE}) = 0$, we obtain $\gamma(T_d) = |\Delta S|(T_d - T_{SE})$ (Fig. S4). For droplets of $R_0 \approx 5\ \mu$m, we measure $T_d - T_{SE} \approx 0.25\ ^\circ$C, which yields $\gamma_d \approx 2.1 \times 10^{-4}$ J/m^2. Plugging these R_0 and γ_d values into Eq. 1, we obtain the $\kappa(R_0^b)$ variation shown in Fig. S6. Having $R_0 \approx 1\ \mu$m for the smallest droplets where buckling is clearly observed yields $R_0^b < 1\ \mu$m. Since κ increases with R_0^b, the $\kappa(R_0^b)$ relation yields an upper limit on κ, $\kappa < 10^4$ k$_B$T (see Fig. S6).

Optical tweezing experiments yield $\kappa > 10^3$ k$_B$T (see above), so that according to Fig. S6, $R_0^b > 0.4\ \mu$m. Combining the estimated limits on κ and R_0^b, as also the simulated[11] $\Gamma_b^{vK} \approx 150$, we obtain the limits on Y in the main text.

While the current analysis neglects possible spontaneous curvature of the frozen monolayer, molecular geometry considerations[4] and the agreement of simulated icosahedral shapes with the experimental ones (Fig. 1 in the main text), justify this approximation.

1. Zarzar LD, et al. (2015) Dynamically reconfigurable complex emulsions via tunable interfacial tensions. Nature 518:520524.
2. Wu XZ, et al. (1993) Surface tension measurements of surface freezing in liquid normal alkanes. Science 261:1018–1021.
3. Tamam L, et al. (2011) Modifcation of deeply buried hydrophobic interfaces by ionic surfactants. Proc. Natl. Acad. Sci. U.S.A. 108:5522–5525.
4. Sloutskin E, et al. (2007) Wetting, mixing, and phase transitions in langmuir-gibbs films. Phys. Rev. Lett. 99:136102.
5. Ocko BM, et al. (1997) Surface freezing in chain molecules: Normal alkanes. Phys. Rev. E 55:3164–3182.
6. Hamster CHS (2013) Deformation of bubbles (Bachelorthesis, Universiteit Leiden, The Netherlands).
7. Ward AD, Berry MG, Mellor CD, Bain CD (2006) Optical sculpture: controlled deformation of emulsion droplets with ultralow interfacial tensions using optical tweezers. Chem. Commun. pp 4515–4517.
8. Brakke KA (1992) The surface evolver. Exp. Math. 1:141–165.
9. Kohyama T, Gompper G (2007) Defect scars on flexible surfaces with crystalline order. Phys. Rev. Lett. 98:198101.
10. Yong EH, Nelson DR, Mahadevan L (2013) Elastic platonic shells. Phys. Rev. Lett. 111:177801.
11. Lidmar J, Mirny L, Nelson DR (2003) Virus shapes and buckling transitions in spherical shells. Phys. Rev. E 68:051910.
12. Bowick MJ, Sknepnek R (2013) Pathways to faceting of vesicles. Soft Matter 9:8088–8095.
13. Dubois M, et al. (2004) Shape control through molecular segregation in giant surfactant aggregates. Proc. Natl. Acad. Sci. USA 101:15082–15087.
14. Dubois M, et al. (2001) Self-assembly of regular hollow icosahedra in salt-free catanionic solutions. Nature 411:672–675.
15. Hirst LS, et al. (2013) Morphology transition in lipid vesicles due to in-plane order and topological defects. Proc. Natl. Acad. Sci. USA 110:3242–3247.
16. Bausch A, et al. (2003) Grain boundary scars and spherical crystallography. Science 299:1716–1718.
17. Gang H, et al. (1998) Macroscopic manifestations of surface crystallization. Europhys. Lett. 43:314–319.
18. Helfrich W (1973) Elastic properties of lipid bilayers - theory and possible experiments. Z.Naturforsch. C 28:693–703.